

# Large Eddy Simulation of a Turbulent Flow over Circular and Mixed Staggered Tubes' Cluster

M. Bedrouni <sup>1</sup>, A. Khelil <sup>1</sup>, M. Braikia <sup>1</sup> and H. Naji <sup>2†</sup>

<sup>1</sup> *University of Chlef, Laboratory of control, Testing, Measurement and Mechanical Simulation, B. P. 151, 2000 Chlef, Algeria*

<sup>2</sup> *University of Artois, University of Lille, IMT Lille-Douai & Yncréa Hauts de France, (LGCgE-ULR 4515), F-62400 Béthune, France*

†Corresponding author email: [hassane.naji@univ-artois.fr](mailto:hassane.naji@univ-artois.fr)

(Received November 1, 2019; accepted January 25, 2020)

## ABSTRACT

A large eddy simulation study was conducted to investigate the turbulent dynamic structure of a fluid flow in two staggered tube configurations, one is composed of all circular cylinders and the second is composed of circular and square cylinders. The present LES, based on the wall-adapting local eddy viscosity model, has been conducted for  $Re_D = 12,858$ , which match available experiments. The appropriate grid has been selected using the grid convergence index method so that the wall-normal coordinate  $y^+$  value is relevant for walls. Streamlines, turbulence kinetic energy contours, instantaneous vorticity contours computed indicate that wake patterns are more chaotic. In addition, flow coherent eddies within both configurations are identified via the  $Q$ -criterion. Based on the obtained findings, it can be stated that the model considered, in addition to being physically sound, demonstrated to be suitable for simulating the turbulent flow over circular and mixed staggered tube bundles with higher resolution.

**Keywords:** Tube bundles; Large eddy simulation; Turbulent flow; WALE model; GCI method;  $Q$ -criterion.

## NOMENCLATURE

$C_w$	WALE constant	$\varepsilon$	absolute error
$D$	cylinder diameter	$\kappa$	Von Karman constant
$e$	relative error	$\nu$	inematic viscosity
$GCI$	grid convergence index	$\nu_t$	SGS eddy-viscosity
$h$	grid spacing	$\rho$	density
$k$	turbulent kinetic energy	$\tau_{sgs}$	deviatoric SGS stress tensor
$P$	Pressure	<b>Superscripts/subscripts</b>	
$Re$	Reynolds number	$i, j, k$	Coordinate alternation index
$S$	strain rate tensor	$t$	turbulent
$S^d$	traceless symmetric tensor	w	wall
$\ S\ $	norm of strain rate tensor	$(\cdot)$	filtered variable
$S_L$	longitudinal pitch-to-diameter ratio	$O^+$	dimensionless quantity
$S_T$	transverse pitch-to-diameter ratio	$(\cdot)'$	fluctuating quantity
$t$	Time	<b>Abbreviations</b>	
$U_{in}$	incoming flow velocity	CFD	computational fluid dynamic
$u_\tau$	wall friction velocity	DNS	direct numerical simulation
$x, y, z$	Cartesian coordinate system	LES	large eddy simulation

$y^+$	wall units coordinate	P/D	pitch-to-diameter ratio
<b>Greek letters</b>		RANS	Reynolds-Averaged Navier-Stokes
$\delta_{ij}$	Kronecker tensor	SGS	subgrid scale
$\Delta$	LES filter length	WALE	wall-adapting local eddy viscosity

## 1. INTRODUCTION

Turbulence is a phenomenon that occurs frequently in fluid flows, both in nature and in almost all industrial flows. In addition, turbulent flows cover up a broad range of temporal and spatial scales whose numerical resolution requires high grid resolution. High resolution and time-dependent simulations can supply detailed predictions of the flow field with unfortunately a very long CPU run time. Currently, efficient numerical simulation methods for predicting unsteady turbulent flows remain limited. This is mainly due to their three-dimensional, unsteady and irregular traits. The most accurate method for solving such flows is direct numerical simulations (DNSs), which handle the Navier-Stokes equations without modelling on a fine grid using a small time step. They are suitable for simple flows, but they become computationally expensive in case of complex flows. Thereby, they are still limited to simple engineering applications or academic studies. The overall cost of a complete calculation is proportional to  $Re$ , which is not suitable for industrial applications where sufficient computer resources are lacking. Thereby, Unsteady Reynolds Averaged Navier-Stokes (URANS) or Large Eddy Simulation (LES) approaches are preferred. LES has come to be regarded as an effective prediction method for turbulent flows. Indeed, it is able to fill gaps URANS approach, as up noted, providing more turbulent information than the URANS method while requiring less computation than the DNS (Duan and Chen, 2015). The choice of one of these methods depends on the targeted physical precision level and available computing resources. This is the LES which is adopted when flow separation prediction, a proper unsteadiness prediction in wake regions, etc. are sought. Such an approach splits flow fields into large and small scales via a filtering procedure. In other words, large eddies are solved while smaller ones (supposed isotropic) are modeled. It is worthy to note that, in this approach, large-scale eddies are the main ingredients that transport momentum into a turbulent flow field. Piomelli (2014) pointed out some current and future aspects of this approach.

The tube bundle geometry gives rise to chaotic and unsteady flow phenomena that lend themselves simulations via LES. Thereby, numerical simulation of such unsteady flows through a tubes bundle is a huge computational challenge. It is worthy to recall that early knowledge on rod bundle flows has come from experimental observations conducted in the seventies. Since then, the fluid flow over a tube bundle has become a problem of the most studied

because of its application in many engineering applications such as flow across overhead cables, flows over skyscrapers, heat exchanger geometries and cooling system for nuclear engineering (nuclear power plant, nuclear fuel rods, etc.). (Wang and Daogang, 2019), Circular cylinders, isolated or in bundles, are commonly seen in the offshore and ocean engineering structures. Subsea pipelines, marine risers and columns of semi-submersibles are salient examples. The flows taking place on these elements are often turbulent and are thereby difficult to handle numerically and experimentally. In other words, comprehensive understanding of phenomena involved in these flows by experimental means has often proved expensive, leading to the numerical methods use as a complementary tool to explain turbulence phenomena occurring over these systems (bundles) (Mikuz and Tiselj, 2016; Salinas-Vázquez *et al.* 2011). Among the many numerical approaches that can be implemented, we can cite the LES method which consists of directly simulating large eddies while modeling the smallest under appropriate conjectures. In practice, many configurations exist yielding the problem very complicated while leading to different flow patterns. The bundle may consist of purely circular tubes, as in heat exchangers, square tubes, as in buildings, or a mixture of tubes (circular and squares or wavy cylindrical), as in electronic component cooling systems and risers and supports offshore platform (Tutar and Hold, 2010). The flow periodicity present in bundles can cause vibrations of the tubes during liquid and acoustic resonance in the fluid flows. Balabani and Yianneskis (1996) have experimentally studied the development of the turbulence structure and mean flow over a bundle composed of three circular tube arrays, one an in-line and two staggered arrays. They established turbulence levels, mean velocities, length and time scales and dissipation rate from ensemble averaged and time resolved laser Doppler anemometry (LDA) measurements. They noted that the interference of adjacent cylinders is stronger in staggered geometries. They also reported that turbulence levels generated by the staggered configuration were higher compared to inline one. Da Silva *et al.* (2019) conducted an LES numerical investigation of a 3D flow on a five-row in-line bundle for the same subcritical Reynolds number. They stated that, in general, their results match to experimental data relating to average velocities and fluctuations over time. Benhamadouche and Laurence (2003) have used LES and transient Reynolds stress transport model (RSTM) in 2D and 3D, at a Reynolds number of  $9 \times 10^3$  with two grid-refined, viz. a coarse and a fine one. They

concluded that 1) the LES results are more consistent with the DNS data and experiments with the fine mesh, and 2) a reasonable agreement can still be achieved with the coarse mesh. Note that, in the latter case, it turned out that the RSTM in 3D had no advantage over the LES.

To our knowledge, few studies on flows past mixed tubes bundles have been performed. Fluid flow over cubes arrays have been studied by Zhengtong and Castro (2006). They performed their computations with two Reynolds numbers, viz.  $5 \times 10^3$  and  $5 \times 10^6$  with the LES and RANS methods. They concluded that, with overly coarse grids, LES is an effective tool for simulating airflow past urban obstacles at high Reynolds number. In addition, they compared the LES and RANS approaches to state that the latter is inadequate, particularly in the canopy region. Oengören and Ziada (1998) compiled experimental data on vortex shedding in a triangle arrangement for the range  $2700 < Re_D < 52,000$ . They found two Strouhal numbers in staggered rows cylinders. Kahil *et al.* (2019) performed a LES of the flow past four cylinders based on the dynamic Smagorinsky model at a sub-critical Reynolds number of  $3 \times 10^3$  and different pitch-to-diameter ratios ( $S_L/D$ ). Their findings revealed that flow structures change with the variation in spacing ( $P/D$ ) and a skewed flow can be detected for some spacing ratios. Chatterjee *et al.* (2010) have studied numerically the flow around five square cylinders. The computations were accomplished for four separation ratios ( $S_T/D = 1.2, 2, 3$  and  $4$ ; with  $S$  and  $d$ , are the transverse spacing and cylinder diameter) in 2D-unsteady incompressible flow at a  $Re$  of 150. The squares were arranged in side-by-side and normal to the on-coming flow. The aim of their study is to investigate and analyze the spacing between cylinders' effect on vortex shedding mechanism and the wake structure. They pointed out that the nature of drag and lift coefficient signals are sinusoidal which ensures that the dominant frequency associated to the vortex shedding is the primary (Strouhal) frequency and the secondary frequency effect is negligible. Furthermore, they reported that, from two successive cylinders, the vortex shedding is similar and when the distance of separation is more than twice the dimension of the cylinders ( $S/D > 2.0$ ), the vortices were in an arrangement of phase opposition. However, when this distance is less than two diameters ( $S/D = 1.2$ ), they reported that there is a deviation of the jets between the cylinders and the wakes merge, resulting in clusters formation. Bakosi *et al.* (2013) presented an LES of the flow in a simplified PWR assembly with  $5 \times 5$  rods. They compared transverse and axial velocity profiles to measures. They found a reorganization of the cross flow which is different from that measured. Lakehal (2018) reported a detailed simulation analysis of turbulent convective flow upward along the heated rods of a PWR sub-channel using a highly-resolved LES approach. He specified that the secondary-flow motion induced by the average flow is responsible for a large portion of the wall-to-flow heat transfer.

In addition, a Very-Large Eddy Simulation (VLES) modeling has been developed and compared to traditional RANS and LES for a flow across a tube bundle by Labois and Lakehal (2011). It has been stated that such an approach is clearly superior to any RANS approach and that it well handles three-dimensional flow unsteadiness. Mikuz and Tiselj (2016) performed a LES of the turbulent flow in a  $5 \times 5$  bar bundle. Their results corroborated the LDV benchmark data pointing that the WALE model is well suit to handle such a geometry.

The present study deals with a large eddy simulation of turbulent flow across circular and mixed tube bundles using the CFD Ansys Fluent 18.1 code (2017) in which the LES is implemented with improved numerical and spatial resolution. The assessment of this simulation is achieved by comparison with the experimental data of Balabani and Yianneskis (1996). This paper starts by summing up research into flow over two different staggered tube bundles, with a particular regard for previous simulations. Then, the governing equations and turbulence modeling are briefly outlined in Section 2 including geometry, boundary conditions, mesh, and the Grid Convergence Index (GCI) method. In Section 3, the main findings are presented and commented. Finally, Section 4 recaps our conclusions.

## 2. GOVERNING EQUATIONS AND TURBULENCE MODELING

### 2.1 Problem Setting and Boundary Conditions

The computational setup consisting of a tubes bundle (cylinders' system) in a square channel is depicted in Fig. 1. The first includes cylinders all of circular shape, while the second configuration is mixed gathering intercalated circular and square cylinders. The mixed bundle consists of six tubes rows (circular and square) arranged in staggered rows with circular cylinders having an outer diameter of 10 mm and square cylinders having a side of 8.86 mm. The transverse and longitudinal pitch to diameter ratios,  $S_T$  and  $S_L$ , are 3.6 and 4.2, respectively. The rods length to diameter ratio is 7.2. Each row comprises 1 or 2 full tubes, as shown in the Fig. 1. Before achieving the targeted simulations, we first used the experimental conditions of Balabani and Yianneskis (1996) to validate our preliminary simulations. The study was carried out at a Reynolds number ( $Re_D = uD/\nu$ ) of 12,858 based on the gap velocity ( $= 1.29 \text{ ms}^{-1}$ ), the cylinder diameter, the working fluid being water at  $20^\circ\text{C}$  whose kinematic viscosity is  $\mu = 1.003 \times 10^{-3} \text{ Pa.s}$  and density is  $\rho = 998.2 \text{ Kg m}^{-3}$ . The rods were rigidly fixed to the upper and lower walls. Using a Doppler Laser Velocimeter technique, the authors measured average velocities and turbulence levels. As shown in Fig. 1, the geometry used in the LES computations is Cartesian

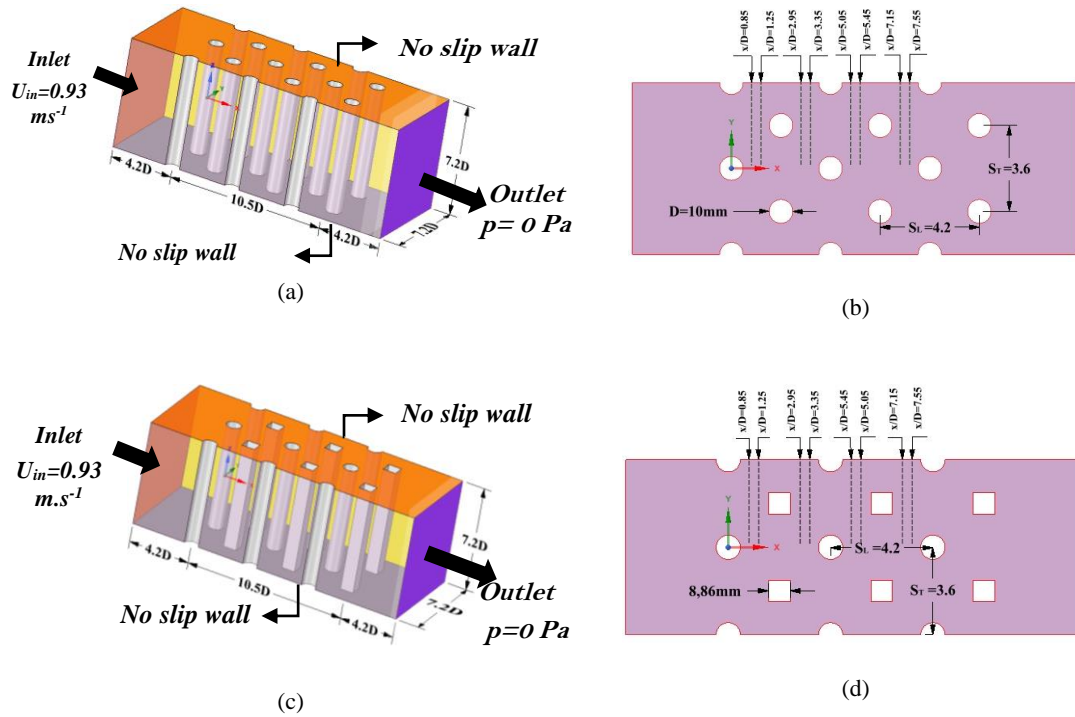


**Fig. 1. Sketch of the computational domain including boundary conditions (not to scale): (a) circular tube bundle, (b)-(d) Cross-sectional views of tubes bundle, and (c) mixed tube bundle.**

(rectangular). The left and right side of the domain are located  $4.2D$  upstream of the first line and downstream of the last row, respectively. They are set as input and output flow boundaries. For these boundaries, a uniform velocity  $U_{\infty}$  ( $= 0.93$  m/s) is prescribed at the inlet and a downstream relative pressure condition ( $\bar{p} = 0$  Pa) is imposed. Its central zone has a length of  $10.5D$ . The top and bottom sides are dealt as stationary no-slip smooth

## 2.2 Turbulence Modeling

The flow, applied to the problem of a staggered tubes bundle consisting of tubes all circular or mixed tubes (circular and square) in cross-flow, is unsteady, turbulent and three dimensional. The fluid is Newtonian and incompressible with constant physical properties and without buoyancy effects. To alleviate this section, only a brief description of the governing equations is provided here. Since the dynamic effect is mainly concerned here, the governing equations are therefore the continuity and momentum equations.

In the LES context, these can be written as follows (Nicoud and Ducros, 1999; Mikuz and Tiselj, 2016; Bennia *et al.* 2016; Medaouar *et al.* 2019) to name a few:

$$\nabla \cdot \bar{U} = 0 \quad (1)$$

$$\frac{\partial \bar{U}}{\partial t} + \bar{U} \cdot \nabla \bar{U} = -\nabla \left( \bar{p} / \rho \right) + \nu \nabla^2 \bar{U} - \nabla \cdot \tau_{sgs} \quad (2)$$

walls ( $\bar{U} = 0$ ), and the cylinders' height is  $7.2D$ , thereby taking up the entire height of the canal. To avoid an excessively large computing mesh, a square section channel with a total length of  $18.9D$  including the 6 rows has been considered herein. It should be stressed that our main target is to simulate such a bundle flow using the LES technique which is briefly described below (see Sub-section 2.2). To sum up, the sketch shown in Fig. 1 illustrates the complete flow simulation area concerned.

Here  $\bar{U}(\bar{u}, \bar{v}, \bar{w})$  and  $\bar{p}$  are the filtered velocity and pressure, respectively,  $\rho$  is the fluid density and  $\nu$  is the fluid's kinematic viscosity, and  $(\cdot)$  denotes any grid-filtered quantity. The small scales influence in Equation 2 appears through the sub-grid scale (SGS) stress tensor which can be defined as follows (Germano *et al.* 1991; Lilly, 1992):

$$\tau_{ij}^{sgs} = \overline{u_i u_j} - \bar{u}_i \bar{u}_j \quad (3)$$

Such a tensor is split into an isotropic part and anisotropic part. The second (deviatoric part), relevant in incompressible flows and reflecting the interaction between resolved and unresolved scales, is modeled (approximated) according to the Smagorinsky-Lilly closure (Germano *et al.* 1991; Lilly, 1992) as follows:

$$\tau_{ij}^{sgs} = -2\nu_t \bar{S} = -2(C_s \Delta)^2 \left\| \bar{S} \right\| \bar{S} \quad (4)$$

wherein  $\Delta = \text{Min}(\kappa y, C_s V^{1/3})$  is the filter length

scale,  $\kappa$  being the Von Karman constant ( $=0.42$ ),  $C_s$  is the parameter that may not be universal (i.e. fixed or dependent on the flow), whose value varies from 0.1 (for shear flows) to 0.2 (for high Reynolds number flows),  $y$  is the closest wall distance,  $V$  is the computational cell volume,

$$\bar{S} = (\nabla \bar{U} + \nabla^T \bar{U}) / 2 \quad (5)$$

$$\text{And } \|\bar{S}\| = (2\bar{S} : \bar{S})^{1/2} \quad (6)$$

$\bar{S}$  being the resolved-scale strain rate tensor,  $\|\bar{S}\|$

the Frobenius norm (second invariant) of  $\bar{S}$ , and  $\nu_t$  is the sub-grid-scale kinematic turbulent viscosity ( $\nu_t = C_k \sqrt{k_{sgs}}$ ,  $k_{sgs}$  being the SGS kinetic energy). The SGS stress tensor's trace is incorporated in the pressure term, thereby modifying the pressure ( $\bar{P} = \bar{p} + \tau_{kk} \delta_{ij} / 3$ ).

For more information on the Smagorinski model and/or its dynamic variant (DSGM), the reader can refer to the ample literature in this area, and in particular to Lilly (1992). Unfortunately, such a model incorrectly handles the near-wall region by providing a non-zero turbulent viscosity at the wall. To fix this imperfection, the van Driest's damping approach is often used, so that the turbulence near the wall has a good parietal behavior, i.e.  $\nu_t \propto y^{+3}$ ,  $y^+ (= y u_\tau / \nu)$  being the dimensionless wall distance.

With an appropriate fine mesh, the Large eddy simulation method using WALE model is found as a pretty accurate tool to simulate turbulent flow in the computational domain as confirmed by Mikuz and Tiselj, 2016; Xia, 2019; Lee *et al.* 2018 and Bennia *et al.* 2020, to name a few. The SGS model adopted here to perform this study is the WALE model (Wall Adapting Local Eddy-Viscosity) in which the SGS eddy viscosity is set in terms of invariants such as (Nicoud and Ducros, 1999; Germano *et al.* 1991; Lilly, 1992):

$$\nu_t = (C_w \Delta)^2 \frac{(\bar{S}^d : \bar{S}^d)^{3/2}}{(\bar{S} : \bar{S})^{5/2} + (\bar{S}^d : \bar{S}^d)^{5/4}} \quad (7)$$

where the traceless symmetric tensor  $\bar{S}^d$  reads (Labois and Lakehal, 2011):

$$S_{ij}^d = (g_{ij}^2 + g_{ji}^2) / 2 - g_{kk}^2 \delta_{ij} / 3 \quad (8)$$

with  $g_{ij}^2 = \bar{u}_i / \partial x_j$ ,  $g_{ij}^2 = g_{ik}^2 g_{kj}^2$ , and  $\delta_{ij}$  is the Kronecker tensor (in terms of components). Here, the Einstein summation convention applies.

The salient points of the relationship (7) are threefold: 1)  $\nu_t$  involves the strain and rotation

tensors, thereby allowing to pick up turbulent structures relevant for the kinetic energy dissipation, 2)  $\nu_t$  automatically tends towards zero near the wall with appropriate scaling ( $\propto y^{+3}$ ), and 3)  $\nu_t$  can be neither negative nor infinite.

It should be recalled that these equations are those of Navier-Stokes, implicitly filtered in space, in which the spatial filter is determined by a filtered computational cell size ( $\Delta$ ). In other words, the process consists in filtering out the small eddies with size smaller than the filter width so that the model can solve only the large scales of the flow field while modeling the small scales.

In our study a value of  $C_w = 0.325$  is used, according to the procedure advised by Nicoud and Ducros (1999), which is taken up in the literature (see, e.g. Mikuz and Tiselj, 2016; Ansys Fluent 18.1 code, 2017) to name a few. According to Busco and Hassan (2018), the WALE model is able to provide a physical insight of secondary flows, and it scales the eddy viscosity appropriately near to walls avoiding any damping function while being less sensitive to the model coefficient  $C_w$ . Moreover, it behaves well to handle wall-bounded flows, is less dissipative, and is able to accurately capture the near wall behavior (in thin shear layer). It is worth noting that it is this model which has been used in this study unless otherwise stated.

### 2.3 Meshing Implementation

It is well accepted that meshing plays a paramount role in carrying out accurate simulations, especially in LES. For this purpose, the grid is not uniform with high density in high gradient zones and low density in less interest zones to minimize the computational effort while getting sufficient accuracy. A structured hexahedral meshing strategy is employed in these simulations using the ANSYS Meshing ICEM CFD meshing. The hexahedral grids are finer in the near-wall regions of the cylinder and the channel and slightly coarse elsewhere as shown in Figs. 2b-d. The distance between the nearest mesh node has been defined such that the maximum value of  $y^+$  is proper ( $\sim 0.87$  for the D grid; see Table 2).

Figures 2(a) and (c) display structured computational grids for the two configurations, while Figs. 2(b) and (d) show the grids around circular and square tubes, respectively. Near to the tube, very fine meshes are required to well resolve the flow physics in the near-wall regions (boundary layer separation and the shedding process). Note that only a reduced number of grid points is displayed to make the figure readable.

### 2.4 Computational Method and Numerical Set-Up

In the present simulation, the finite volume method is applied to compute Eqs. (1)-(2) with appropriate boundary conditions using the ANSYS FLUENT CFD code 18.1. A bounded central differentiation

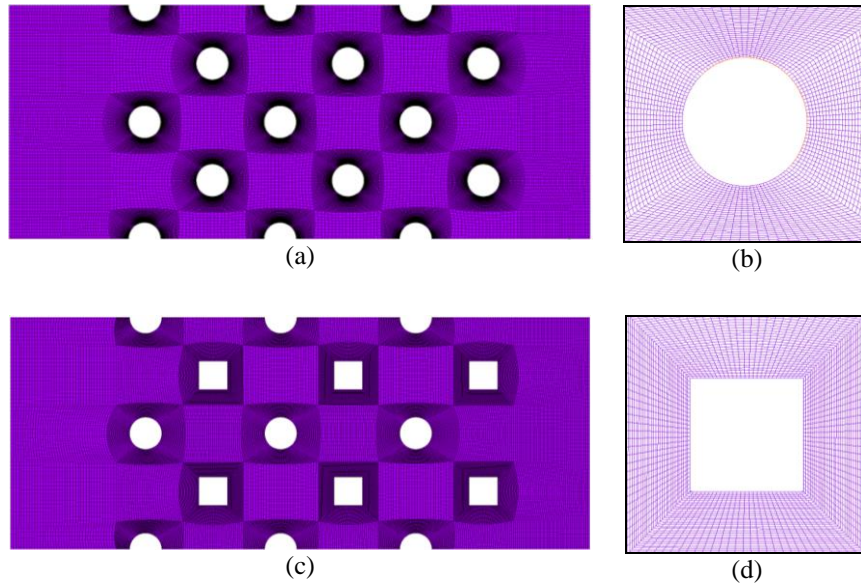


**Fig. 2. Mesh topology:** (a) Computational grid of circular tube bundle, (b) Computational domain of mixed tube bundle, (c) grid close-up around the circular tube, (d) grid close-up around the square tube.

**Table 1 Simulation settings and boundary conditions (BCs)**

Settings parameters	
Simulation type	3D Unsteady
SGS model	Wale model
Pressure-velocity coupling	SIMPLEC
Momentum discretization scheme	Bounded central differencing
Convergence criterion	$10^{-5}$
Fluid Properties	$\mu = 1.003 \times 10^{-3} \text{ Pa}\cdot\text{s}$ ; $\rho = 998.2 \text{ Kg}\cdot\text{m}^{-3}$ at $T = 20 \text{ }^\circ\text{C}$
Cylinder diameter	$D = 10^{-2} \text{ m}$
$Re$	12,858
Time step	$10^{-3} \text{ s}$
Grid used	4859,712 cells
CFD code	Ansys Fluent 18.1
BCs	
Inlet	Inlet velocity: $U_\infty = 0.93 \text{ m}\cdot\text{s}^{-1}$
Outlet	Relative pressure: $0 \text{ Pa}$
All walls	No-slip wall: $\overline{U} = 0$

scheme is used for momentum discretization, while a second order implicit scheme is involved to advance the equations in time. The well-known SIMPLEC algorithm is used to handle the pressure-velocity coupling between momentum and continuity equations. A convergence criterion of  $10^{-5}$  has been set for the continuity and momentum equations residuals with a time step of  $10^{-5} \text{ s}$ . To sum up, Table 1 gathers further details.

Four different grids size are used to check the solution independency from the grid quality and cell size. The details of these grids, which all have a

hexahedral structure, are settled in Table 2. Some of these meshes may seem a bit coarse for traditional LES. However, it is worth recalling that the main intent here is to assess the model capacity considered to handle such flows even if the resolution is rather low.

Simulations have been performed for the first configuration where the tubes all have a circular shape and validated by comparison with the experimental results of [Balabani and Yianneskis \(1996\)](#).

**Table 2 Grid sizes and properties**

Grid	Cell size	y <sup>+</sup> min	y <sup>+</sup> "average	y <sup>+</sup> max
Grid A (coarse)	505,800	0.93	5.23	12.5
Grid B (medium)	1519,800	0.26	2.35	5
Grid C (fine)	3618,480	0.23	0.71	1.02
Grid (very fine)	4859,712	0.14	0.42	0.87

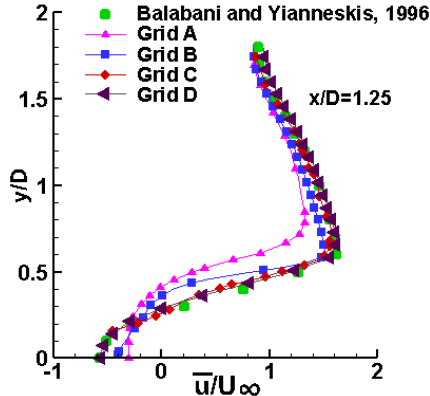


**Fig. 3. Spanwise profiles of the normalized average streamwise velocity; grid sensitivity.**

The Fig. 3 shows y-variations of the normalized average streamwise velocity for four grids at x/D=1.25. Computations on the first three grids show that the streamwise velocity is getting closer to experimental data as the number of cells increases. However, the results remain almost constant with increasing grid size from grid C to grid D without significant change occurring.

To estimate the uncertainty due to the mesh and to quantify the discretization error for the first three grids (B, C, D), the Grid Convergence Index (GCI) method is performed herein. This is a practical method of accounting for numerical uncertainty based on the generalized Richardson extrapolation (GRE) to estimate the percentage of discretization error (Roache, 1997; Coleman and Stern, 1997; Salpeter and Hassan, 2012; Karimi *et al.* 2012; Khelil *et al.* 2016). Its principle takes the following steps:

- rate the grid refinement ratio  $r$  and the formal convergence order  $p$  using the following relationships:

$$r_{21} = h_2 / h_1 \text{ and } r_{32} = h_3 / h_2 \quad (9)$$

$$p = \frac{1}{\ln(r_{21})} \left| \ln \left| \frac{\epsilon_{32}}{\epsilon_{21}} \right| + \ln \left( \frac{r_{21}^p - s}{r_{32}^p - s} \right) \right| \quad (10)$$

with  $s = \text{sign}(\epsilon_{32} / \epsilon_{21})$ .

Specify that  $\epsilon_{21}$  and  $\epsilon_{32}$  are the absolute error between two solutions viz  $f_1, f_2$  and  $f_2, f_3$ , respectively, computed on two different grids with uniform discrete spacings,  $h_1$  and  $h_2$ ,

corresponding to a fine and coarse grid spacing, while  $r$  is the grid refinement ratio, and  $p$  stands for the precision order of the discretization scheme. It is worth noting that  $f_1$  being the fine grid solution,  $f_2$  is the middle grid solution and  $f_3$  is the coarse grid solution.

• **Numerical Uncertainty Quantification**

The numerical uncertainty quantification can be handled using the Roache's GCI method (Roache, 1997; Coleman and Stern, 1997; Salpeter and Hassan, 2012; Karimi *et al.* 2012; Khelil *et al.* 2016). In this approach, the GCI index can be expressed as follow:

$$GCI^{21} = \frac{C_a}{r_{21}^p - 1} e_a^{21} \times 10^2 \quad (11)$$

where  $r_{21}^p = (h_2 / h_1)^{1/d}$ ,  $d$  being the grid dimension,  $C_a$  is an adjustment factor that has been set at 1.25, and  $e_a^{21}$  is the approximate relative error ( $= \epsilon_{21} / f_1$ ). It should be reported that between grids 2 and 3, the same relationships take place. In addition, according to Roache (1997), at least three levels of grid refinement (coarse, medium, and fine) should be selected to determine the convergence appropriate order while ensuring that numerical predictions are within an asymptotic range.

**Table 3 GCI method results**

Grid	medium/fine (B/C)	fine/very fine (C/D)
Mesh refinement indices	$r_{21}^p = 1.33$	$r_{32}^p = 1.10$
Absolute errors	$\epsilon_{21} = 0.25$	$\epsilon_{32} = 0.021$
Convergence order	$p = 3.52$	$p = 3.52$
Extrapolated value	$f_{ext}^{21} = 1.36$	$f_{ext}^{32} = 1.70$
Relative errors	$e_a^{21} = 16.66$	$e_a^{32} = 1.21$
GCI %	$GCI^{21} = 11.78$	$GCI^{32} = 1.70$

Table 3 gathers the results for the drag coefficient on the last tubes used as a grid independence check variable for such an approach.

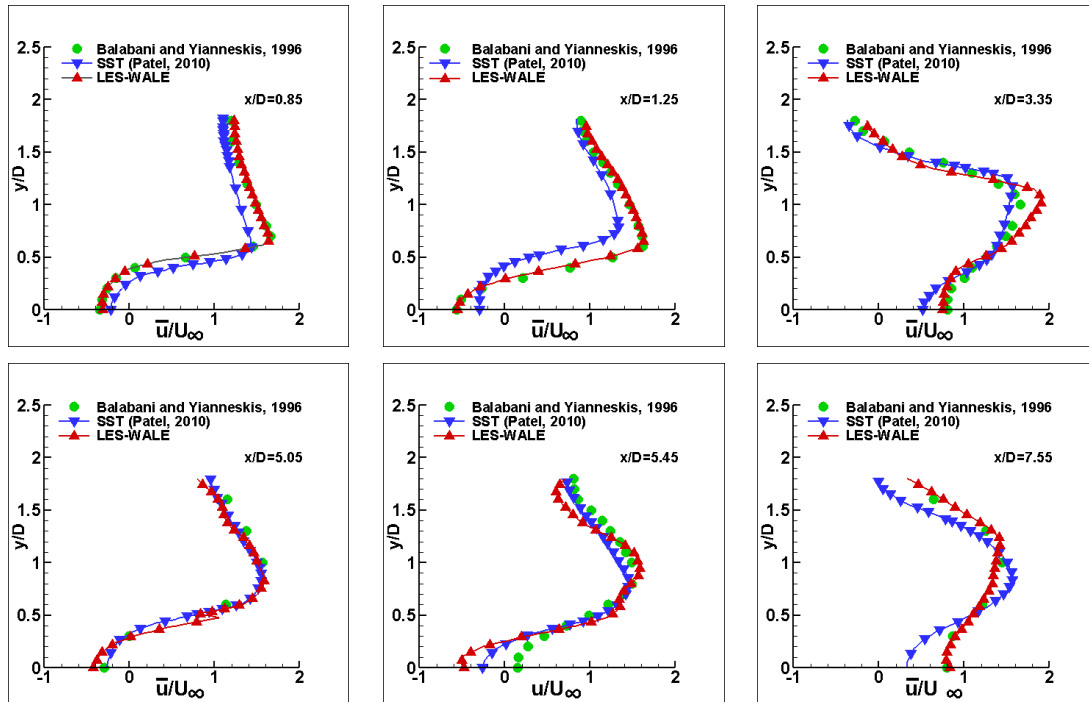


**Fig. 4.** Streamwise dimensionless average velocity profiles ( $\bar{u}/U_\infty$ ) compared with experimental data and the SST model (Patel, 2010) at selected axial locations and  $z = 0$ .

From this Table 3, it can be seen that the error due to the refinement from the coarse to medium grid is of the order of 12%, whereas it is 1.7% (small value) for the refinement from medium to fine grid indicating that the obtained solution is in a proper range. Thereby, the results presented in the remainder of this paper are achieved with the very finest grid, viz. the D grid.

### 3. COMPUTATIONAL RESULTS AND DISCUSSION

Three-dimensional simulations have been performed for both configurations on the finest D-grid using the WALE model. The primary target of this study is to simulate the mean flow Balabani and Yianneskis (1996) for the circular staggered tubes bundle to assess the methodology and subsequently the flow features. The results are also compared with those of Patel (2010), achieved via a numerical simulation with the SST model. After model validation, the two configurations are compared in terms of velocities, flow patterns and turbulences quantities.

#### 3.1 Velocity Distributions and Flow Patterns

The time-averaged and dimensionless mean streamwise and spanwise velocities are compared to the measurements taken at locations highlighted in Figs. 1b and 1d, viz.,  $x/D = 0.85, 1.25, 3.35, 5.05, 5.45,$  and  $7.5$ . Comparisons are made-up between our LES predictions, (Patel, 2010) and Balabani and

Yianneskis (1996) data (see Figs. 4 and 5). As can be seen in Fig. 4, it is the WALE model which well predicts better the streamwise velocity ( $\bar{u}/U_\infty$ ) whatever the location  $x/D$ . Note that this velocity sometimes becomes negative at some stations, indicating that an inverse flow occurs. As for the transverse velocity ( $\bar{v}/U_\infty$ ), it is globally better predicted by the LES model than the SST model (see Fig. 5). It can be seen that, from the third station, both models exhibit rather significant deviations. At the fifth and sixth rows ( $x/D = 5.05$  and  $5.45$ ), the spanwise velocity is greatly overestimated by the SST model. However, at the station  $x/D = 7.55$ , the LES results agree better with Balabani and Yianneskis data compared to SST results which yet overestimate this velocity when  $y/D > 1$ . In addition, since the average GCI is small ( $GCI < 1.7\%$ , see Table 3), one can state that the numerical uncertainty due to a discretization error does not contribute significantly to the disagreement between the predicted  $\bar{u}$ - and  $\bar{v}$ -velocities via the WALE model and the experimental data. Furthermore, it should be stressed that the wall-normal coordinate  $y^+$  is such that  $0.14 \leq y^+ \leq 0.87$  for the cylinders walls and  $0.27 \leq y^+ \leq 1.08$  for the channel walls. Thereby, through these findings, it can be already stated such preliminary results support the WALE model.

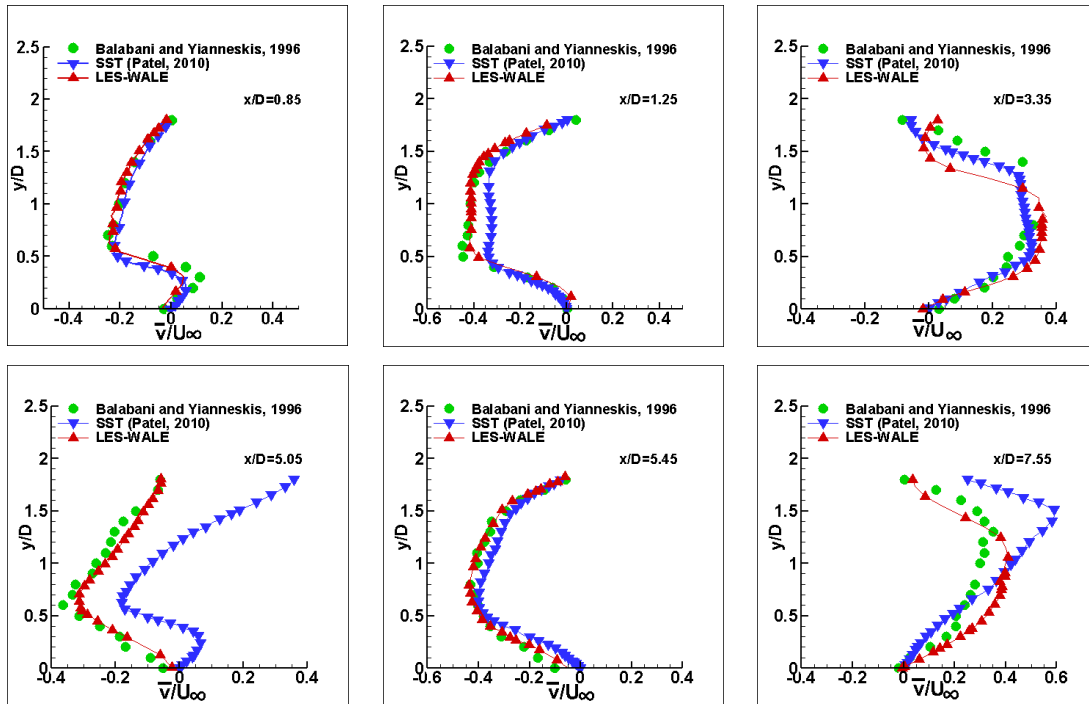


Fig. 5. Transverse dimensionless average velocity profiles ( $\bar{v} / U_{\infty}$ ) compared with experimental data and the SST model (Patel, 2010) at selected axial locations and  $z = 0$ .

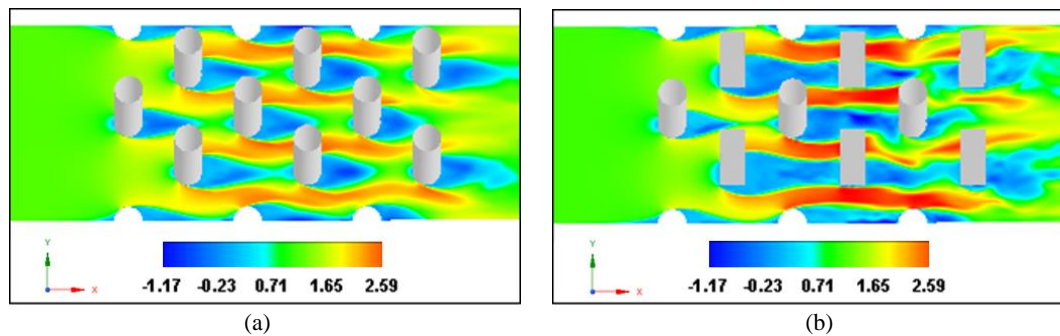


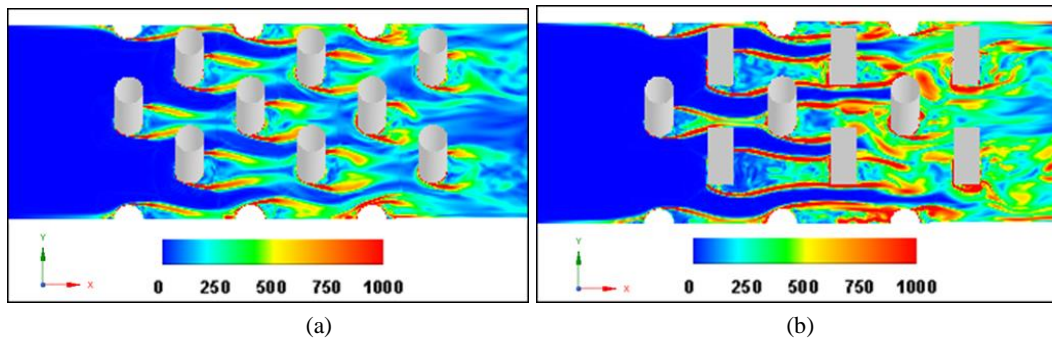
Fig. 6. Dimensionless time-averaged streamwise velocity in  $x - y$  plane at  $z = 0$  (midplane) for circular (a) and mixed tubes bundles (b).

Figure 6 shows dimensionless time-averaged streamwise velocity contours for both configurations at the plane  $z = 0$ . It is found that the interference between the tubes is greater in the mixed configuration compared to the purely circular configuration. In addition, we observe that the introduction of square-row tubes speeds up the flow and results in a larger recirculation zone. Inverse velocities are higher in the mixed tube bundle and the shedding occurs in the tubes wake as expected. The highest velocities are between the tubes and the lowest are in the tubes wake. At the exit, the flow rate is decelerated due to the absence of inhibiting flow in the next tubes row.

Figure 7 shows the vorticity magnitude at the same time to better visualize the shedding process. It appears clear that the most important rotational

structures in the flow occur in the mixed configuration in which the flow vortex starts from the wake up to the adjacent tube. Regions of relatively high vorticity magnitude are observed behind the first and second rows downstream. However, their intensity decreases when the last row is reached.

Figure 8 depicts the velocity vector while showing the development of recirculation zones of different sizes in the wake region. Explicitly, recirculation zones appear at the top and bottom of the square cylinders of the second bundle. In total, six recirculation zones can be identified behind the first squares: one at the top, one at the bottom, two near the bottom edge of the square and two others before the next square, due to the interference between the square tubes. The vortices behind the square



**Fig. 7. Instantaneous Vorticity magnitude contours in  $x - y$  plane at  $z=0$  for  $t=10 s$  around circular (a) and mixed tubes bundles (b).**

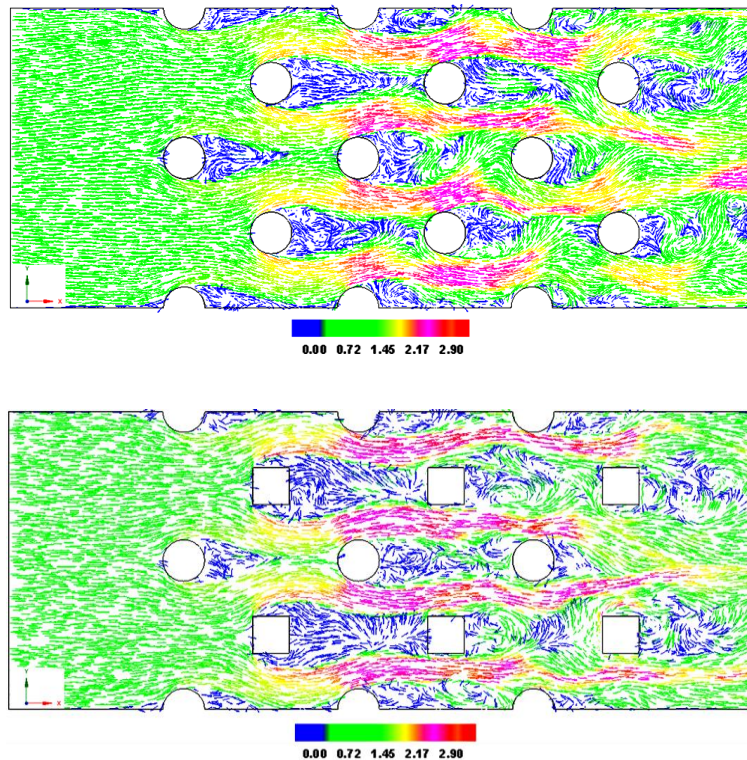


**Fig. 8. Averaged velocity vector contours around circular and mixed tube bundles in  $x - y$  plane at  $z=0$ .**

cylinders are stronger and bigger than behind the circular cylinders in all rows. Once the flow passes the first square cylinders, the upper and lower vortices disappear from the next square cylinders. In the circular tube bundle, two main vortices develop in the wake region without interaction between the cylinders. For both configurations, it is set up that the flow reversal is more pronounced downstream of the first and second rows of cylinders.

Figure 9 shows the distribution of the normalized time-averaged velocity along the spanwise direction ( $y - z$  plane) for both configurations at the position of  $x/D = -1.2$  (before any obstacle),  $x/D = 2.9$  (behind the first row tubes),  $x/D = 7.1$  (behind the second row tubes) and the last stations at

$x/D = 11.3$  (behind the third row tubes). The first streamwise slices contours, without any obstacle, are similar, indicating that there is no tubes upstream effect on the flow. At the second and third stations, the streamwise velocity distribution points periodic repeats along the spanwise direction for both models. At these stations, compared to the purely circular model, the streamwise velocity is assessed to be greater in the mixed model, because of the different flow separation characteristics for the different square cylinders. Further downstream of the station  $x/D = 11.3$ , the velocity parallel distribution ceases according to the spanwise direction, and the flow rate decelerates.

The streamlines plot of the full flow field shown in Figure 10 demonstrate that purely circular cylinder

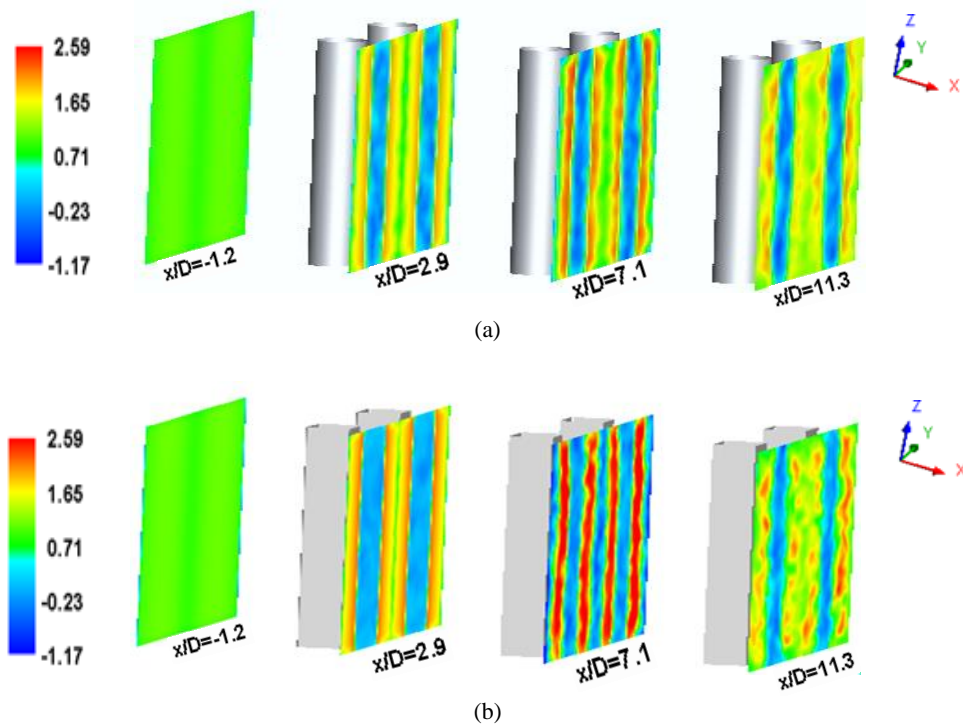


**Fig. 9. Dimensionless time-averaged streamwise velocity distributions in  $y-z$  plane at different locations  $x/D$ : (a) circular and (b) mixed tube bundles.**

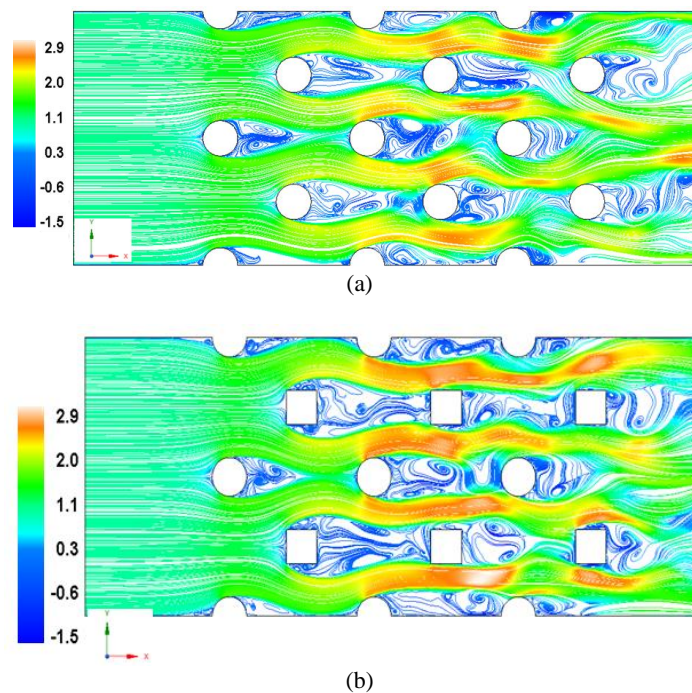


**Fig. 10. Streamlines colored by time-averaged streamwise velocity in  $x-y$  plane at  $z=0$  around (a) circular and (b) mixed tube bundles.**

arrays give rise to a more stable and organized flow pattern with less fluctuation. However, the introduction of square cylinders in the bundle results in a more chaotic flow. It is noticed that the

recirculation regions become gradually small in the streamwise direction, and the recirculation length in the mixed model is bigger.

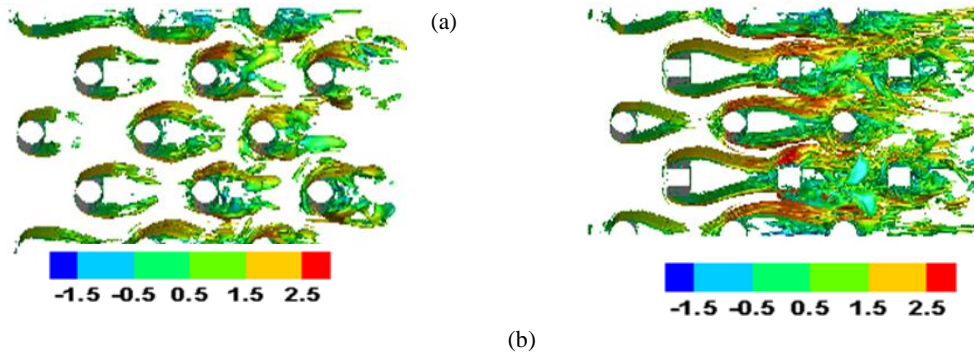


Fig. 11. Instantaneous iso-surface vorticity colored with the streamwise velocity around (a) circular and (b) mixed tube bundles at  $z=0$  and  $t=10$  s .

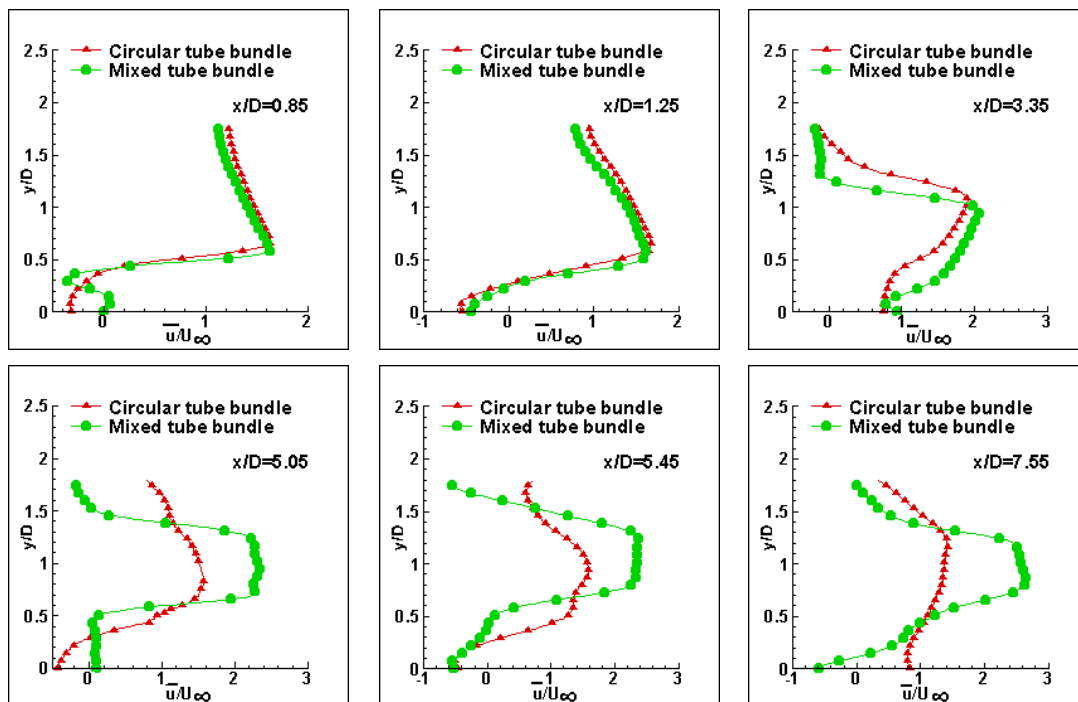


Fig. 12. Dimensionless time averaged streamwise velocity comparison between the two bundles.

Figure 11 depicts the iso-surfaces of the instantaneous vorticity magnitude in the flow for the two models. It can be seen an extremely complex flow distribution in the wake flow for the mixed configuration. In addition, the turbulent structures extent in the mixed model appears to be higher. Thereby, the iso-vorticity contours demonstrate the LES ability to capture full flow motion thus indicating that the adopted LES model is suited to handle complex turbulent flow through tubes bundles.

Figure 12 compares the dimensionless time-averaged streamwise velocity in the two bundles. It can be seen that, for the first two locations, the streamwise velocity is similar because of the presence of the same obstacles and that the flow has not yet reached the square cylinders. There is no effect upstream of these two sites. At the third and fourth stations, the flow is more accelerated

between mixed tubes and decelerated near the square due to the reverse flow. the same phenomena are observed at stations  $x/D = 5.05$  and  $5.45$ . In addition, for distant stations ( $x/D > 5$ ), the maximum velocity is higher (almost twice) in the mixed configuration compared to the circular tube bundle.

In Fig. 13, the normalized mean transverse velocity for the two tube bundles are compared at the same selected axial locations as the streamwise velocity. For the first three stations, this velocity exhibits almost similar profiles. Beyond, profiles differ. Explicitly, from  $x/D = 3.35$  to  $5.45$ , the transverse velocity for the mixed bundle is higher than circular tubes bundle for  $y/D < 1$ . When the flow is closed to the next cylinder row ( $y/D > 1$ ), the transverse velocity is decreased with a higher gradient in mixed configuration. For last two stations,

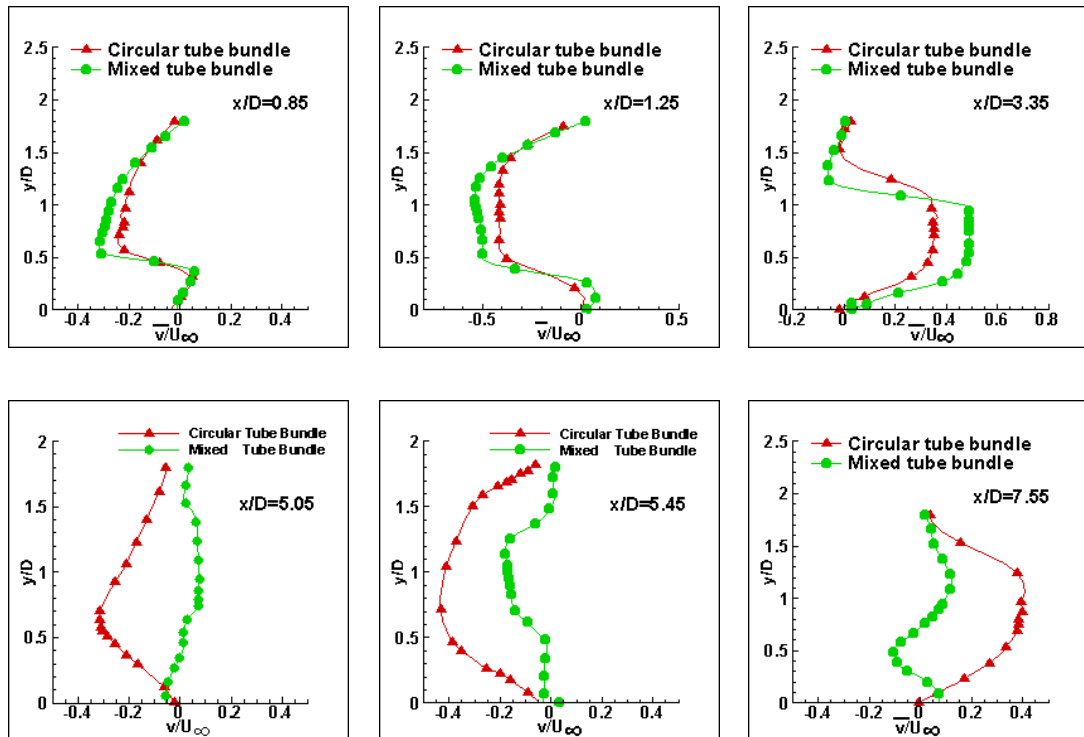


Fig. 13. Dimensionless time averaged transverse velocity comparison between the two bundles.

transverse velocity is higher in circular tubes bundle. Note that its maximum in the last station is  $\approx 0.15$  for the mixed bundle and  $\approx 0.4$  for the circular bundle.

### 3.1.1 Turbulence Kinetic Energy, Anisotropy Degree and Eddies Identification

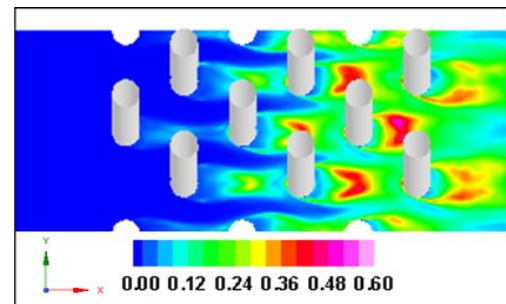
The normalized resolved turbulent kinetic energy (tke) is defined in terms of the SGS stress tensor trace as (Jahrul and Luke, 2018) to cite a few:

$$k_{sgs}^+ = \overline{0.5u_i' u_i'} / U_\infty^2 = 0.5\overline{\tau_{ii}^{sgs}} / U_\infty^2 \quad (12)$$

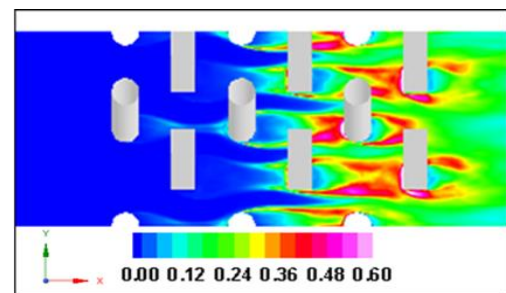
using summation notation, and  $u_i'$  is the SGS part of the non-filtered velocity  $u_i$ . Note that a transport equation for  $k$  can then be derived via the trace of the transport equation for the SGS stress tensor, while modeling the diffusion and dissipation terms.

Figure 14 presents the normalized turbulence kinetic energy contours in mid-plane  $z$ . It appears that in both configurations, the distribution of turbulent energy is very different in the last rows, involving more vortices in the mixed configuration. This energy is generated in the wake regions and then dissipated gradually in the mainstream flow. Downstream of the first two rows of cylinders, the tke is very low, then is increased downstream of the other rows due to the strongest eddies to reach its maximum value found downstream of fourth and fifth rows. The intensity of the turbulent flow structures being greater in the mixed model, a

vibration could occur.



(a)



(b)

Fig. 14. Dimensionless resolved tke contours around circular tube bundle (a) and mixed tube bundle (b) in  $x-y$  plane at  $z=0$ .

Figure 15 depicts the dimensionless distribution of  $|\overline{v'u'}|$ . These contours provide an indication of the

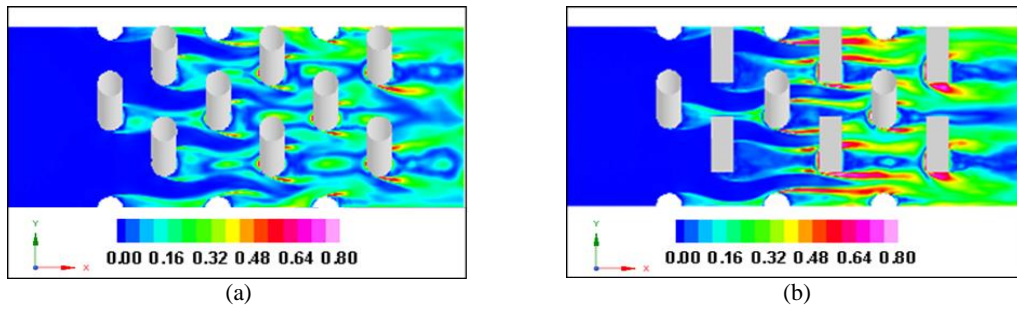


Fig. 15. Turbulence anisotropy via  $|v'-u'|$ -dimensionless contours around circular tube bundle (a) and mixed tube bundle (b) in  $x-y$  plane at  $z=0$ .

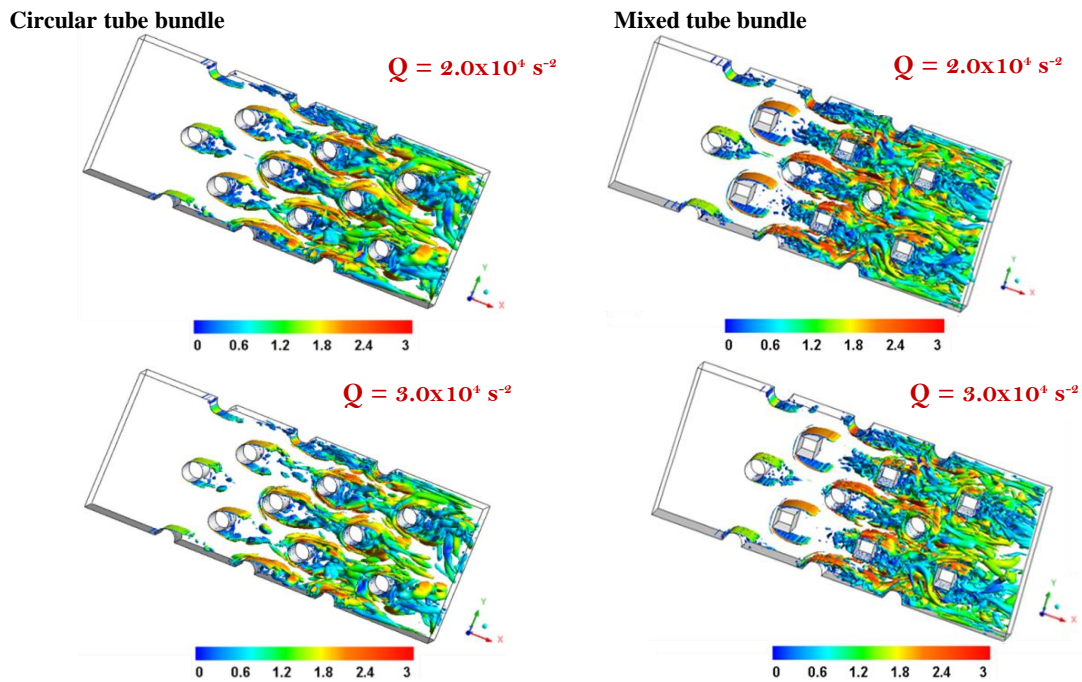


Fig. 16. Coherent eddies via the  $Q$  – criterion's iso-surface within both configurations at  $t=10 s$  coloring by the velocity magnitude.

turbulence anisotropy degree. Downstream of the first two lines, the anisotropy is weak, whereas it increases downstream of the other rows, except for the last one. To sum up, the mixed arrangement exhibits a larger gap between the two velocities root mean square (rms) pointing out that the flow is more anisotropic than in the purely circular model.

In what follows, the coherent three-dimensional vortices can be identified via the criterion  $Q$  which is none other than the second invariant of the gradient tensor ( $\nabla \bar{U}$ ) defined as follows:

$$Q = \left( \|\Omega\|^2 - \|S\|^2 \right) / 2 \quad (13)$$

It provides the relative dominance of either the

rotation rate or the strain rate while advisedly involving the smallest resolved scales in an LES. In other words,  $Q > 0$  indicates the region where the vorticity magnitude outweighs that of the strain-rate, while  $Q < 0$  indicates the opposite. In addition, The  $Q$ -size typifies the eddies energy. Note that [Dubief and Delcayre \(2000\)](#) pointed out its superiority on the low-pressure criterion in wall-bounded turbulent flows.

The iso-surfaces plot of coherent eddies is depicted in Fig. 16 for both configurations at various instants. It shows different structures deduced via the  $Q$ -criterion and colored by the velocity magnitude. It reveals a set of coherent eddies in the flow evolving irregularly throughout the tubes bundle, stretching due to high velocity gradients and

distorting in hairpin and/or horseshoe shapes from the first and second rows. It appears that the mixed configuration involves many and strong eddies with higher density, especially for the larger  $Q$  value ( $3 \times 10^4 \text{ s}^{-2}$ ). From the third row, the density and distortion degree of the iso-vortex surfaces increase in both configurations, highlighting the strongly turbulent character of these areas, and thereby, confirming the unveiling of Figs. 14 and 15.

#### 4. CONCLUSION

The present study deals with the time-dependent computations of the flow through a staggered purely circular and mixed tubes bundle using large eddy simulation. Moreover, the GCI method is used to assess the grid refinement influence on the solution. It turned out that the adopted LES demonstrates that mean streamwise and transverse velocities predicted reasonably corroborate the available experimental data. In addition, the quantities obtained with the LES-WALE model are in better agreement with the experimental data compared with those of the SST model. For the two configurations, a reverse flow occurs in the wake region and flow perturbations, due to the unsteady nature of the vortex shedding, are more prominent in the square than circular cylinders. Furthermore, the analysis of the flow features demonstrates that the mixing between the circular and square tubes results in instable and disorganized flow pattern with interference between tubes while exhibiting a more chaotic flow. In addition, the velocity increases in the mixed configuration compared to that with circular tubes. Finally, among the two arrangements, it is the mixed which exhibits a more anisotropic flow with many and more intense eddies. From the stability point of view, it is the circular tube bundle that is often advised. However, to better generate coherent structures which are generally associated with heat transfer, the mixed bundle can be used to improve cooling efficiency. The latter deserves further study.

#### REFERENCES

- ANSYS Fluent Theory Guide* - Fluent 18.1 (2017).
- Bakosi, J., M. A. Christon, R. B. Lowrie, R. R. Pritchett-Sheats and L. A. Nourgaliev (2013). Large-eddy simulations of turbulent flow for grid-to-rod. *Nuclear Engineering and Design* 262, 544-561.
- Balabani, S. and M. Yianneskis (1996). An experimental study of the mean flow and turbulence structure of cross-flow over tube bundles. *Proceedings of the Institution of Mechanical Engineers* 210, 317-331.
- Benhamadouche, S. and D. Laurence (2003). LES, coarse LES, and transient RANS comparisons on the flow across a tube bundle. *International Journal of Heat and Fluid Flow* 24, 470-479.
- Bennia, A., H. Fellouah, A. Khelil, L. Loukarfi and H. Naji (2020) Experiments and Large-Eddy Simulations of Lobed and Swirling Turbulent Thermal Jets for HVAC's Applications. *Journal of Applied Mathematical Modelling* 13, 103-117.
- Bennia, A., L. Loukarfi, A. Khelil, S. Mohamadi, M. Braikia and H. Naji (2016). Contribution to the Experimental and Numerical Dynamic Study of a Turbulent Jet Issued from Lobed Diffuser. *Journal of Applied Mathematical Modelling* 9(6) 2957-2967.
- Busco, G. and Y. A. Hassan (2018). Space and energy-based turbulent scale-resolving simulations of flow in a 5x5 nuclear reactor core fuel assembly with a spacer grid. *International Journal of Heat Fluid Flow* 71, 420-441.
- Chatterjee, D., Biswas, G. and A. Sakir (2010). Numerical simulation of flow past row of square cylinders for various separation ratios. *Computers & Fluids* 39, 49-59.
- Coleman, H. W. and F. Stern (1997). Uncertainties and CFD validation. *Journal of Fluids Engineering* 119(4), 795-803.
- da Silva, B. L., R. D. Luciano, J. Utzig and H. F. Meier (2019). Analysis of flow behavior and fluid forces in large cylinder bundles by numerical simulations. *International Journal of Heat Fluid Flow* 75, 209-226.
- Duan, G. and B. Chen (2015). Large eddy simulation by particle method coupled with sub-particle-scale model and application to mixing layer flow. *Applied Mathematical Modelling* 39, 3135-3149.
- Dubief, Y. and F. Franck Delcayre (2000). On coherent-vortex identification in turbulence. *Journal of Turbulence* 1(1), 1-22.
- Germano, M., U. Piomelli, P. Moin and W. H. Cabot, (1991). A dynamic subgrid-scale eddy viscosity model. *Physics of Fluids* 3(7), 1760.
- Jahrul, M. A. and L. P. J. Fitzpatrick (2018). Large eddy simulation of flow through a periodic array of urban-like obstacles using a canopy stress method. *Computers & Fluids* 171, 65-78.
- Kahil, Y., S. Benhamadouche, A. S. Berrouk and I. Afgan (2019). Simulation of subcritical-Reynolds-number flow around four cylinders in square arrangement configuration using LES. *The European Journal of Mechanics - B/Fluids* 74, 111-122.
- Karimi, M., G. Akdogan, K. H. Dellimore and S. M. Bradshaw (2012). Quantification of numerical uncertainty in computational fluid dynamics modelling of hydrocyclones. *Computers and Chemical Engineering* 43, 45-54.
- Khelil, A., H. Naji, L. Loukarfi, M. Hadj Meliani and M. Braikia (2016). Using numerical simulation to deepen understanding of the

- interaction of multiple turbulent swirling jets mounted with unbalanced positions. *Journal of Applied Mathematical Modelling* 40, 3749-763.
- Labois, M. and D. Lakehal (2011). Very-Large Eddy Simulation (V-LES) of the flow across a tube bundle. *Nuclear Engineering and Design* 241, 2075-2085.
- Lakehal, D. (2018). Highly-resolved LES of turbulent convective flow along a PWR rod bundle. *International Journal of Heat Mass Transfer* 122, 785-794.
- Lee, S. L., S. Lee and Y. A. Hassan (2018). Numerical investigation of turbulent flow in an annular sector channel with staggered semi-circular ribs using large eddy simulation. *International Journal of Heat Mass Transfer* 123, 705-717.
- Lilly, D. (1992). A proposed modification of the Germano subgrid-scale closure method. *Physics of Fluids* 4, 633.
- Medaouar, W., L. Loukarfi, M. Braikia, A. Khelil and H. Naji (2019). Experimental and Numerical Study of a Turbulent Multiple Jets Issued from Lobed Diffusers. *Journal of Applied Mathematical Modelling* 12(3), 729-742.
- Mikuz, B. and I. Tiselj (2016). Wall-resolved Large Eddy Simulation in grid-free 5x5 rod bundle of MATIS-H experiment. *Nuclear Engineering and Design* 298, 64-77.
- Nicoud, F. and F. Ducros (1999). Subgrid-scale stress modelling based on the square of the velocity gradient tensor. *Flow, Turbulence and Combustion* 62, 183-200.
- Oengören, A. and S. Ziada (1998). An in-depth study of vortex shedding, acoustic resonance and turbulent forces in normal triangle tube arrays. *Journal of Fluids and Structures* 12, 717-758.
- Patel, Y., (2010). *Numerical Investigation of Flow Past a Circular Cylinder and in a Staggered Tube Bundle Using Various Turbulence Models*. Master's thesis, Department of Mathematics and Physics, Lappeenranta University of Technology, 53850 Lappeenranta, Finland.
- Piomelli, U. (2014). Large eddy simulations in 2030 and beyond. *Philosophical Transactions of the Royal Society A* 372, 20130320.
- Roache, P. J. (1997). Quantification of uncertainty in computational fluid dynamics. *Annual Review of Fluid Mechanics* 29, 123-160.
- Salinas-Vázquez, M., M.A. de la Lama, W. Vicente and E. Martínez (2011). Large Eddy Simulation of a flow through circular tube bundle. *Journal of Applied Mathematical Modelling* 35, 4393-4406.
- Salpeter, N. and Y. Hassan (2012). Large eddy simulations of jet flow interaction within staggered rod bundles. *Nuclear Engineering and Design* 251, 92-101.
- Tutar, M. and A. E. Hold (2010). Computational modelling of flow around a circular cylinder in subcritical flow regime with various turbulence models. *International Journal for Numerical Methods in Fluids* 35 (7),763-784.
- Wang, H. and L. Daogang, (2019). Large eddy simulation on the turbulent flow and mixing in a 2x2 rod bundle. *Annals of Nuclear Energy* 549-561.
- Xia, Y. (2019). *Prediction of Thermoacoustic Instability in Gas Turbine Combustors*. PHD thesis, Imperial College London. May 2019 London, U.K.
- Zhengtong, X. and I. P. Castro (2006). LES and RANS for turbulent flow over arrays of wall-mounted obstacles. *Flow, Turbulence and Combustion* 76, 291-312.